


# Geometry of Almost-Conserved Quantities in Symplectic Maps


## Part II. Recovery of approximate invariant

T. Zolkin 

*Independent Researcher, Chicago, IL*

S. Nagaitsev 

*Brookhaven National Laboratory, Upton, NY 11973 and  
Old Dominion University, Norfolk, VA 23529*

I. Morozov 

*Synchrotron Radiation Facility “SKIF”, Koltsovo 630559, Russia and  
Novosibirsk State Technical University, Novosibirsk 630073, Russia*

S. Kladov 

*University of Chicago, Chicago, IL 60637*

(Dated: June 12, 2025)

Noether’s theorem, which connects continuous symmetries to exact conservation laws, remains one of the most fundamental principles in physics and dynamical systems. In this work, we draw a conceptual parallel between two paradigms: the emergence of exact invariants from continuous symmetries, and the appearance of approximate invariants from discrete symmetries associated with reversibility in symplectic maps. We demonstrate that by constructing approximating functions that preserve these discrete symmetries order by order, one can systematically uncover hidden structures, closely echoing Noether’s framework. The resulting functions serve not only as diagnostic tools but also as compact representations of near-integrable behavior.

The second article applies the method to global dynamics, with a focus on large-amplitude motion and chaotic systems. We demonstrate that the approximate invariants, once averaged, accurately capture the structure of resonances and the boundaries of stability regions. We also explore the recovery of exact invariants in integrable cases, showing that the method reproduces the correct behavior when such structure is present. A single unified function, derived from the map coefficients, yields phase portraits, rotation numbers, and tune footprints that closely match numerical tracking across wide parameter ranges. Comparisons with the Square Matrix method reveal that while both approaches satisfy local constraints, our technique provides greater accuracy and robustness in resonant and strongly nonlinear regimes. These results highlight the method’s practical power and broad relevance, offering a compact, analytic framework for organizing nonlinear dynamics in symplectic maps with direct applications to beam physics and beyond.

### I. INTRODUCTION

The first part of this study developed a systematic perturbative method for constructing approximate invariants in symplectic maps — discrete systems closely related to Hamiltonian dynamics and widely applicable across mathematical and physical problems [1–3]. These invariants are not only conserved up to a given order but also respect two families of discrete symmetries induced by reversibility [4]. In continuous-time dynamics, Noether’s theorem [5] establishes a correspondence between symmetries of the action and exact integrals of motion; here, we uncover a similar correspondence in the discrete setting.

By benchmarking our method against results from Lie algebra technique and by probing the structure of low-order resonances, we demonstrated both the mathematical consistency and practical accuracy of the approach in

the vicinity of a fixed point. In this second part, we shift the focus from foundational formulation to broader applications. Much like the classical Arnold scheme in KAM theory [6–8], as the order of approximation increases, the simply connected domain where the approximate invariant holds shrinks toward a point. In this limit, the system approaches an integrable twist map — the same map that lies at the heart of Lie algebra benchmarking. However, our interest lies beyond this infinitesimal regime: we aim to extend the method into the realm of large-amplitude dynamics.

On one end, we investigate near-integrable systems exhibiting chaos beyond the fixed point neighborhood. In such cases, the method uncovers coherent structures — such as chains of islands — that are otherwise obscured by standard twist expansions of action-angle variables. On the other end, we revisit known integrable maps and test whether the method can recover their exact global invariants. This is a critical test: failure in the integrable case would cast doubt on capturing global features in chaotic systems, where no exact invariant exists.

---

\* iguanodyn@gmail.com

We begin where the first part left off, by briefly restating the method for general planar maps. The remainder of this article is organized as follows. In Section III, we test the method on all known integrable maps with smooth invariants for transformation in McMillan form [9], systematically described by Suris [10]. For maps with finite polynomial invariants, our results fully recover the expected structure; for maps whose invariants are infinite power series, we observe almost-everywhere convergence. In Section IV, we examine the method's limitations by applying it to chaotic systems, focusing on the quadratic and cubic Hénon maps [11]. They are relatively well understood [12–14], yet exhibit rich nonlinear dynamics, making them ideal for benchmarking new methods against known results. These maps are directly relevant to accelerator physics, modeling horizontal dynamics in lattices with thin sextupole and octupole lenses [15, 16]. We use several case studies where the phase space contains large island chains, analyzing both the approximate invariants and the nonlinear rotation number derived from them, providing an alternative to traditional twist expansion. In Subsection IV B, we extend this analysis to the joint space of dynamical variables and map parameters, constructing approximations of the simply connected domain of validity. Building on recent work [Fractal], where integrable systems were shown to approximate the geometry of resulting fractal structures to first nonlinear order, we demonstrate that the perturbative approach enables further refinement — albeit with limitations — beyond the fixed points/ $n$ -cycles framework.

One crucial component of this method is the averaging procedure, which resolves under-determinacy in the expansion coefficients and ensures resonance compatibility (i.e., applicability at rational rotation numbers). As a case study, we compare this to the naive alternative of setting all undetermined coefficients to zero. Along the way, we draw comparisons with other analytical tools, particularly the Square Matrix (SM) method, and show how even low-order approximations can capture essential features of strongly nonlinear systems.

In the following and final part of this series, we demonstrate its effectiveness by applying it to realistic dynamical models corresponding to accelerator lattice configurations from the FermiLab complex. As we show, this construction naturally extends the classic Courant-Snyder [17] formalism — a foundational framework in accelerator physics now spanning seven decades and historically focused on linear phenomena. This limitation stemmed from several factors: weak nonlinearities at small amplitudes, design goals favoring linearity, and the limited analytical tools available at the time (1953), preceding the full development of KAM theory and later progress in chaotic dynamics. While this is not the first attempt to describe near-integrable motion using normal forms, we believe the present approach holds promise for broader applications due to its conceptual simplicity.

## II. PERTURBATION METHOD

Consider a map of the plane  $T: \mathbb{R}^2 \mapsto \mathbb{R}^2$ , which is symplectic (i.e., it preserves area and orientation) and admits a power series expansion:

$$\begin{aligned} q' &= A_{1,0} q + A_{0,1} p + A_{2,0} q^2 + A_{1,1} q p + A_{0,2} p^2 + \dots, \\ p' &= B_{1,0} q + B_{0,1} p + B_{2,0} q^2 + B_{1,1} q p + B_{0,2} p^2 + \dots \end{aligned}$$

- We begin by introducing a general polynomial ansatz for the approximate invariant of order  $n$ :

$$\mathcal{K}^{(n)}[p, q] = \mathcal{K}_0 + \epsilon \mathcal{K}_1 + \dots + \epsilon^n \mathcal{K}_n,$$

where  $\mathcal{K}_m$  is a homogeneous polynomial of degree  $(m+2)$ :

$$\mathcal{K}_m[p, q] = \sum_{\substack{i,j \geq 0 \\ i+j=m+2}} C_{i,j} p^i q^j.$$

To determine the coefficients  $C_{i,j}$ , we require that the approximate invariant be conserved up to  $\mathcal{O}(\epsilon^{n+1})$ :

$$\mathcal{R}_n = \mathcal{K}^{(n)}[p', q'] - \mathcal{K}^{(n)}[p, q] = \overline{\mathcal{R}_n} \epsilon^{n+1} + \mathcal{O}(\epsilon^{n+2}).$$

The lowest-order contribution, which can also be derived via standard linearization, is defined only up to a constant multiplier

$$\mathcal{K}_0[p, q] = C_0 [A_{0,1} p^2 + (A_{1,0} - B_{0,1}) p q - B_{1,0} q^2]. \quad (1)$$

The *seed* coefficient  $C_0$  can be set to unity or chosen specifically to eliminate resonant denominators.

- Due to under-determinacy, the invariant (after all two-indexed coefficients  $C_{i,j}$  have been fixed) is known only up to a series:

$$C_0 \mathcal{K}_0 + C_1 \mathcal{K}_0^2 + \dots$$

Nevertheless, the approximate invariance condition holds to the required order, and the twist coefficient  $\tau_k$  converges at order  $n = 2k + 2$ .

- The remaining coefficients  $C_k$  (for  $k > 0$ ) are obtained via the *averaging procedure*, which minimizes the residual error. After transforming to the eigenbasis of the Jacobian,  $(q, p) \rightarrow (Q, P)$ , the linear part of the map becomes a pure rotation, and the zeroth-order invariant takes the form

$$\mathcal{K}_0[P, Q] = P^2 + Q^2.$$

The coefficients  $C_k$  are then determined by solving another system of linear equations

$$\frac{d}{dC_k} I_n = 0,$$

where the integral

$$I_n = \int_0^{2\pi} \overline{\mathcal{R}_n}^2[\rho, \psi] d\psi.$$

Here,  $(\rho, \psi)$  are polar phase space coordinates defined by  $Q = \rho \cos \psi$  and  $P = \rho \sin \psi$ .

### III. RECOVERY OF INTEGRABLE SYSTEMS

In the first part of this manuscript, we explored various examples demonstrating that knowledge of the twist coefficients alone is insufficient to reconstruct the full invariant of motion, as the coefficients  $C_k$  remain undetermined. Before venturing into applications for chaotic systems, it is essential to validate our perturbative approach and the averaging procedure on systems that possess an exact invariant of motion. Since the PT was specifically designed to approximate such invariants, integrable systems provide an ideal testing ground.

Fortunately, the McMillan form of the map, explored in the first part of this manuscript, is not only one of the simplest forms of a planar transformation, offering significant flexibility in its dynamics through various choices of force functions, but it is also inherently symplectic and reversible, exhibiting clear symmetries for any force function  $f(p)$ , not necessarily analytical. Furthermore, for this form of the map, Suris' theorem [10] provides significant constraints on the possible forms of the invariant when it is assumed to be an analytic function.

**Theorem 1 (Yu. B. Suris)** *Consider the McMillan form mapping  $(q, p) \mapsto (p, -q + f(p))$  over the field of complex numbers  $\zeta = (q, p) \in \mathbb{C}^2$ , where  $f(p)$  is holomorphic in some band of finite width (independent of  $\epsilon$ ) about the real axis. Then it has a nontrivial symmetric integral  $\mathcal{K}[p, q]$ , holomorphic in the domain  $|p - q| < \delta_0$ , in the following and only in the following three cases:*

$$\begin{aligned} \text{(I): } \quad \mathcal{K}[p, q] &= A p^2 q^2 + B (p^2 q + p q^2) \\ &\quad + \Gamma (p^2 + q^2) + E p q + \Delta (p + q), \\ \text{(II): } \quad \mathcal{K}[p, q] &= A e^{\alpha p} e^{\alpha q} + B (e^{\alpha p} + e^{\alpha q}) \\ &\quad + \Gamma (e^{\alpha p} e^{-\alpha q} + e^{-\alpha p} e^{\alpha q}) \\ &\quad + \Delta (e^{-\alpha p} + e^{-\alpha q}) + E e^{-\alpha p} e^{-\alpha q}, \\ \text{(III): } \quad \mathcal{K}[p, q] &= \Lambda_1 (\cos[\omega p - \psi] + \cos[\omega q - \psi]) \\ &\quad + \Lambda_2 \cos[\omega (p + q) - \phi] \\ &\quad + \Lambda_3 \cos[\omega (p - q)]. \end{aligned}$$

Here  $A, B, \Gamma, \Delta, E, \Lambda_{1,2,3}, \alpha, \omega, \psi$  and  $\phi$  are arbitrary constants (guaranteeing the absence of singularities for  $f(p)$  in the neighborhood of the real axis).

#### A. Symmetric McMillan map

The first invariant corresponds to the *symmetric integrable McMillan map* [9, 18], which has a polynomial form that is biquadratic in  $p$  and  $q$ . This specific structure of the exact invariant naturally aligns with the polynomial form of our approximate invariant. For transformations with a fixed point at the origin ( $\Delta = 0$ ), the invariant

can, in almost all cases ( $\Gamma \neq 0$ ), be rewritten in a simplified form [15, 16]:

$$\mathcal{K}_I[p, q] = \text{C.S.} + \beta \Pi \Sigma + \alpha \Pi^2. \quad (2)$$

We adopt the symmetric notation  $\Sigma = p + q$ ,  $\Pi = p q$ , and define  $\mathcal{K}_0[p, q] \equiv \text{C.S.} = \Sigma^2 - r_2 \Pi$ . The resonant denominators are denoted as  $r_{1,2} = a \mp 2$ ,  $r_3 = a + 1$ , and  $r_4 = a$ . For full details, see the first part of the manuscript. The corresponding force is given by a rational function:

$$f_I(p) = -\frac{\beta p^2 - a p}{\alpha p^2 + \beta p + 1}.$$

In this section,  $\alpha$  and  $\beta$  refer to mapping parameters, not to the Twiss parameters. In this simplified setting, the dynamics are governed by two intrinsic quantities. The first is the trace  $a$ , which determines the bare tune  $2\pi\nu_0 = \arccos(a/2)$ . The second is the ratio  $\beta^2/\alpha$ , which characterizes the nonlinearity and directly influences the first twist coefficient  $\tau_0$ , given by [15, 16]

$$2\pi\tau_0 = -\frac{\alpha}{r_1 r_2} \left[ 3r_4 + (a + 8) \frac{r_3}{r_1} \frac{\beta^2}{\alpha} \right].$$

By introducing the small parameter  $\epsilon$ , we obtain the following Taylor series of  $f$ :

$$f(q) = a q - r_3 \beta \epsilon q^2 + (r_3 \beta^2 - r_4 \alpha) \epsilon^2 q^3 + \dots$$

From this expansion, we construct the approximate invariant:

$$\begin{aligned} \mathcal{K}^{(n)}[p, q] &= \text{C.S.} + \beta \Pi \Sigma \epsilon + [\alpha \Pi^2 + C_1 \text{C.S.}^2] \epsilon^2 \\ &\quad + 2\beta C_1 \Pi \Sigma \text{C.S.} \epsilon^3 \\ &\quad + [C_1 (\beta^2 r_2 \Pi^3 + (2\alpha + \beta^2) \Pi^2 \text{C.S.}) + C_2 \text{C.S.}^3] \epsilon^4 \\ &\quad + \mathcal{O}(\epsilon^5). \end{aligned}$$

While the first three terms match the exact invariant, Eq. (2), all additional terms are proportional to  $C_i$ . The application of the averaging procedure ensures that for any order  $n > 1$  and all  $i > 0$ , the coefficients  $C_i$  must vanish in order to satisfy  $dI_n/dC_i = 0$ . Thus, this demonstrates that PT with averaging successfully “passes” its first test — showing exact convergence once the appropriate order is reached.

#### B. Suris exponential mapping

Next, we turn to the Suris mapping with the exponential invariant (II). As in the previous case, the invariant can be significantly simplified by imposing a fixed point at the origin and requiring  $\mathcal{K}[0] = 0$ :

$$\begin{aligned} \mathcal{K}_{II}[p, q] &= -a \sinh(p) \sinh(q) \\ &\quad + 2\beta [\sinh(p + q) - \sinh(p) - \sinh(q)] \\ &\quad + 2\alpha [2 \cosh(p) \cosh(q) - \cosh(p) - \cosh(q)]. \end{aligned}$$

Furthermore, if  $\alpha \neq 0$ , the invariant can be rescaled so that  $\alpha = 1$ , leaving only two intrinsic parameters.

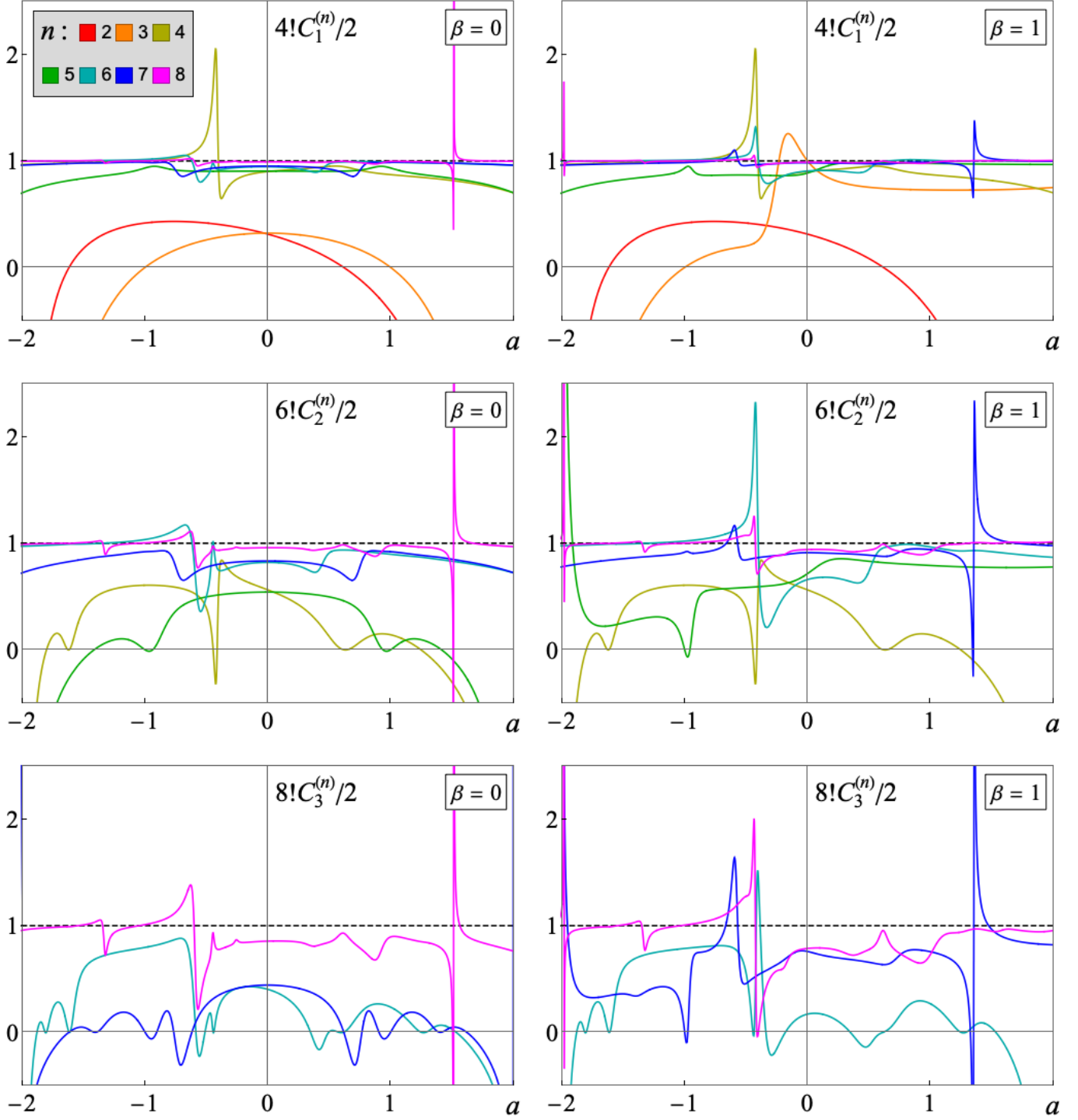


FIG. 1. The first three coefficients  $C_i^{(n)}$  ( $i = 1, 2, 3$ ) obtained using the averaging procedure for the Suris exponential mapping are shown as functions of the map parameter  $a$  (colored curves, as indicated in the legend). All coefficients are normalized as  $(2(i+1))!C_i^{(n)}/2$  and should be compared to the reference value of unity (represented by the dashed black line). The left and right columns display two sample cases: an odd mapping ( $\beta = 0$ ) and a mapping with mixed nonlinearity ( $\beta = 1$ ). As expected, for the odd mapping in odd orders,  $C_i^{(n)}$  are even functions of  $a$ .

In this form, the force function simplifies to

$$f_{\Pi}(p) = \log \frac{(1 + a/4) e^{2p} - (1 - \beta) e^p + (1 - \beta - a/4)}{(1 + \beta - a/4) e^{2p} - (1 + \beta) e^p + (1 + a/4)},$$

which we again expand in a Taylor series:

$$ap - r_3 \beta \epsilon p^2 + \left( r_3 \beta^2 - r_4 \frac{10 - a^2}{12} \right) \epsilon^2 p^3 + \dots$$

Next, we compare the approximate invariant obtained before applying the averaging procedure

$$\begin{aligned} \mathcal{K}_{\Pi}^{(n)}[p, q] = & \text{C.S.} + \beta \Pi \Sigma \epsilon + C_1 \text{C.S.}^2 \epsilon^2 + \frac{10 - a^2}{12} \Pi^2 \epsilon^2 \\ & + \beta \frac{r_3 \Pi + (24 C_1 - 1) \text{C.S.}}{12} \Pi \Sigma \epsilon^3 + C_2 \text{C.S.}^3 \epsilon^4 \\ & + \Pi^2 \epsilon^4 \left[ \beta^2 \frac{(12 C_1 - 1)(r_2 \Pi + \text{C.S.})}{12} \right. \\ & \left. + \frac{(23 - 2a^2)(r_4 \Pi - \text{C.S.}) + 60 C_1(10 - a^2) \text{C.S.}}{6!/2} \right] \\ & + \mathcal{O}(\epsilon^5), \end{aligned}$$

with the power series expansion of the actual invariant

$$\begin{aligned} \mathcal{K}_{\Pi}[p, q] = & \text{C.S.} + \beta \Pi \Sigma \epsilon + \frac{\text{C.S.}^2}{12} \epsilon^2 + \frac{10 - a^2}{12} \Pi^2 \epsilon^2 \\ & + \beta \frac{r_3 \Pi + \text{C.S.}}{12} \Pi \Sigma \epsilon^3 + \frac{\text{C.S.}^3}{360} \epsilon^4 \\ & + \frac{r_4(23 - 2a^2) \Pi + 3(9 - a^2) \text{C.S.}}{6!/2} \Pi^2 \epsilon^4 \\ & + \mathcal{O}(\epsilon^5). \end{aligned}$$

From this comparison, we extract the exact values of the coefficients

$$C_i = \frac{2}{[2(i+1)]!}, \quad i = 0, 1, 2, \dots$$

These coefficients are independent of the mapping parameters and, unlike in the symmetric McMillan map case, do not vanish. Moreover, summing all terms of the form  $C_i \text{C.S.}^{i+1}$  gives a closed expression:

$$\sum_{i=0}^{\infty} C_i \text{C.S.}^{i+1} = 2 (\cosh \sqrt{\text{C.S.}} - 1).$$

Since coefficients  $C_{i,j}$  can be determined exactly, our focus remains on understanding  $C_i^{(n)}$ , which are obtained via the averaging procedure. In general, these coefficients depend on both  $a$  and  $\beta$ . For example,

$$\begin{aligned} C_1^{(2)} &= \frac{5}{48} \frac{r_5}{r_1 r_2}, \\ C_1^{(3)} &= \frac{r_3}{30 r_2} \frac{7 r_1 r_4^2 r_6 S_0 S_1 + 6 r_4 S_2 \beta^2 + 180 r_2 r_3 S_3 \beta^4}{5 r_1^2 r_4^2 S_0^2 - 24 r_1 r_3 r_4 S_0 S_4 \beta^2 + 72 r_3^2 S_3 \beta^4}, \end{aligned}$$

where

$$\begin{aligned} S_0 &= 10 - a^2, & S_3 &= 5 + 2a + 3a^2, \\ S_1 &= 23 - 2a^2, & S_4 &= 3 + 2a, \\ S_2 &= 761 + 561a - 385a^2 - 315a^3 + 29a^4 + 24a^5. \end{aligned}$$

Since  $C_i^{(n)}$  are not required to obtain the power series  $\nu(J)|_{J=0}$ , which describes the dynamics in a simply connected region around the origin, our goal is to attempt a reconstruction of the full invariant of motion that extends globally. To illustrate our findings, we refer to Figs. 1 and 2.

Fig. 1 shows the coefficients  $C_i^{(n)}$  obtained at different orders ( $n \leq 8$ , shown as colored curves) as functions of the trace parameter  $a$ . A uniform scaling is applied to all curves so that the value of  $C_i$  is normalized to unity (dashed black line). Each row corresponds to a different  $i$ , displaying  $C_1^{(n)}$ ,  $C_2^{(n)}$  and  $C_3^{(n)}$ , respectively. The two columns represent different values of the nonlinear parameter: the left column,  $\beta = 0$ , represents an odd-force function, while the right column,  $\beta = 1$ , reflects a mixed (odd and even) nonlinearity. The plots show that although  $C_i^{(n)}$  depends on both parameters, it increasingly approximates a constant value as  $n$  grows, approaching unity in the expected limit.

One key difference from the previously considered integrable McMillan map is that, in this case, convergence is not expected at any finite order. Instead, the behavior suggests that the infinite series sum appears to *converge almost everywhere*, resembling the Gibbs phenomenon observed in Fourier series for square, triangular, and other discontinuous functions.

**Observation.** Notably, none of the coefficients exhibit singularities within the parameter range corresponding to a stable fixed point at the origin ( $|a| < 2$ ). This aligns with expectations, as Suris mappings lack nonlinear resonances, except for special degeneracies where  $r_3 = 0$  or  $r_4 = 0$ ; this stands in contrast to generic chaotic systems, where almost each rational value of  $\nu_0$  corresponds to a resonance at the origin — either a singular one, such as a touch-and-go bifurcation, or a non-singular, e.g.,  $k$ -island chain. Moreover, as the order increases, errors become increasingly localized, and their width progressively narrows.

Fig. 2 further explores this behavior by mapping  $C_i^{(n)}$  across both parameters  $a$  and  $\beta$ . Rows correspond to different orders  $n = 2, \dots, 8$ , while columns represent different values of  $i = 1, \dots, 4$ . The same rescaling as in Fig. 2 is applied, with dark blue indicating a reference value of 1. The convergence can be observed as, (i) for a given  $i$  and increasing  $n$ , the regions of large error, highlighted in yellow, become increasingly localized, while simultaneously, (ii) the color map undergoes rescaling, reflecting an improved overall approach to unity. With that, we consider another test to be “passed” — albeit in the limit  $n \rightarrow \infty$ . The results for the trigonometric Suris mapping exhibit qualitatively similar behavior, as the two cases are inherently related.

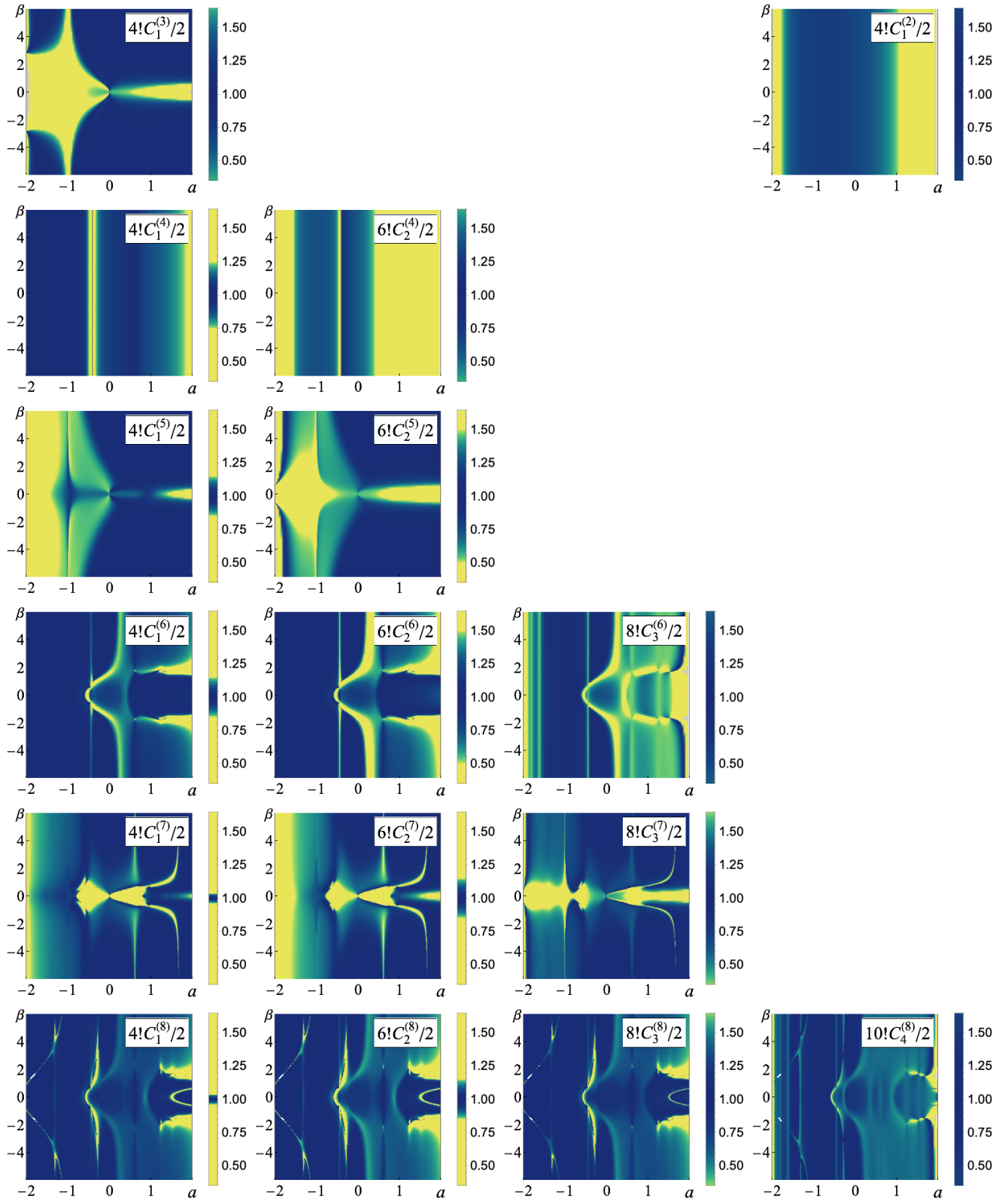


FIG. 2. Coefficients  $C_i^{(n)}$  obtained using the averaging procedure for the Suris exponential mapping are shown as functions of the map's parameters,  $a$  and  $\beta$ , with values represented by the color map. The different columns correspond to  $i = 1, \dots, 4$ , while the rows represent  $n = 3, \dots, 8$ ; for a more compact presentation, the plot for  $C_1^{(2)}$  is placed in the top right corner. All coefficients are normalized as  $(2(i+1))!C_i^{(n)}/2$  and should be compared to unity (shown in dark blue). Note that for a given  $i$ , the color map is progressively rescaled with increasing  $n$  to better illustrate convergence.

#### IV. APPLICATIONS TO CHAOTIC SYSTEMS

In this section, we explore various applications of our perturbative approach using the chaotic quadratic and cubic Hénon maps [11]. Owing to the wealth of existing analytical results (see, e.g., [12–14]), these systems serve as an excellent test ground. Both transformations can be written in McMillan form, with force functions given by  $f(p) = ap + p^2$  and  $f(p) = ap + p^3$  respectively.

We begin with a few specifically selected examples and discuss the approximation of the nonlinear rotation number. We then extend our study to the joint space of phase-space variable and mapping parameter, using our perturbative technique to describe the intricate structure of the fractal stability diagram. Afterward, we subject the square matrix (SM) method to the same test, enabling a direct comparison.

Finally, in Appendix A, we present the level sets of the approximate invariants for all three cases discussed in Subsection IV A. These are intended for readers’ independent exploration, although we include brief commentary and a complementary set of figures produced using the SM method, Appendix B.

##### A. Nonlinear rotation number

As the rotation number is an intrinsic dynamical quantity, its accurate evaluation remains a central challenge. In the nearly (quasi-)integrable example discussed at the end of the first part of this series (Subsection II E, Fig. 14), we showed how  $\nu(J)$  can be extracted under favorable conditions. However, in more realistic scenarios — where the phase space features prominent island chains and extensive chaotic regions — the action variable becomes less practical to use. Moreover, evaluating the action numerically is non-trivial, complicating meaningful comparisons between analytical and numerical approaches.

A partial remedy comes from considering the rotation number as a function of the phase space coordinates themselves, rather than  $J$ . In this formulation, we can directly compute  $\nu(\mathcal{K}[p, q])$  from the approximate invariants via Danilov’s theorem. Furthermore, numerical orbit tracking naturally yields  $\nu[p_0, q_0]$  as a function of initial conditions, facilitating direct comparison. In accelerator physics, this approach aligns well with practical measurements, where the nonlinear betatron tune is inherently observed as a function of the particle’s position and momentum.

Fig. 3 presents three examples drawn from the family of Hénon cubic (I, II) and quadratic (III) maps. Here, we consider non-resonant bare tune values  $\nu_0$ , setting these cases apart from those in Subsection II D of the first part. The values of the trace parameter  $a$  are chosen to lie near low-order resonances —  $1/4$ ,  $1/3$ , and  $1/5$  for cases I through III, respectively — so that the island chains can still be captured by relatively low-order perturbative expansions.

The top row of Fig. 3 shows phase space portraits colored using the REM indicator, which highlights resonance structures: dark blue corresponds to quasi-linear motion, cyan to quasi-integrable, and gray to chaotic or unstable initial conditions. Below, we plot the rotation number as a function of the initial coordinate along the first symmetry line  $l_1$ , i.e.,  $(q_0, p_0) = q_1(1, 1)$ , using both numerical orbit tracking (black thick curves) and results extracted from non-averaged approximate invariants (with  $C_i = 0$ ) and averaged (denoted A). The second row presents the rotation number on the same scale as the corresponding phase space plots, while the two bottom rows show zoomed-in regions (highlighted with white rectangles) for better clarity.

Focusing on these magnified views, we again observe the clear advantage of the averaging procedure. In case I, for example, non-averaged approximations fail to capture the separatrix associated with the  $1/4$  island chain (which appears as a plateau at  $\nu = 1/4$ ), despite correctly predicting the twist coefficient. In contrast, the averaged second-order curve (orange) already provides a reasonable approximation, while higher-order terms further improve the result — accurately reproducing the steep frequency drop near the separatrix, which often resembles a local collapse. This is precisely the situation where low-order approximations  $\nu_k$  offer a better qualitative and quantitative description than both the non-averaged case and the Lie power series  $\nu(J)$ .

In cases II, III the benefit of averaging remains clear. A comparison of the second-order curves (orange) in both cases shows that averaging produces significantly more accurate results. In particular, for case II, the curves corresponding to orders 8 (purple) and 10 (brown) closely match the numerically computed rotation number inside the entire 6-island chain (comprising a pair of 3-cycles).

As a further check, we include in Appendix A the level sets of the averaged invariants used to compute the rotation numbers shown here — see Figs. 9, 10, and 11 for completeness. In case I, we observe that for  $n \geq 4$ , the PT provides a highly accurate description of the inner chain of four islands. As the order  $n$  increases, additional features corresponding to higher-period orbits begin to emerge. Although these features may appear to “fluctuate” between successive orders, the overall boundary of stability is captured reasonably well. In case II, the situation is similar: the chain of six islands (representing two groups of 3-cycles) becomes clearly resolved at  $n = 8$ . While PT again begins to break down at larger amplitudes, as in case I, the relatively low-order approximation not only captures the island chain but also succeeds in extending beyond the separatrix by a non-negligible distance. It is worth noting that, while we focus here on the simply connected region inside the largest inner chain, Danilov’s theorem can be applied to the outer level sets surrounding the origin as well. Case III presents the most challenging scenario. Even so, the  $n = 7$  approximation yields interesting results, successfully revealing all of the islands.

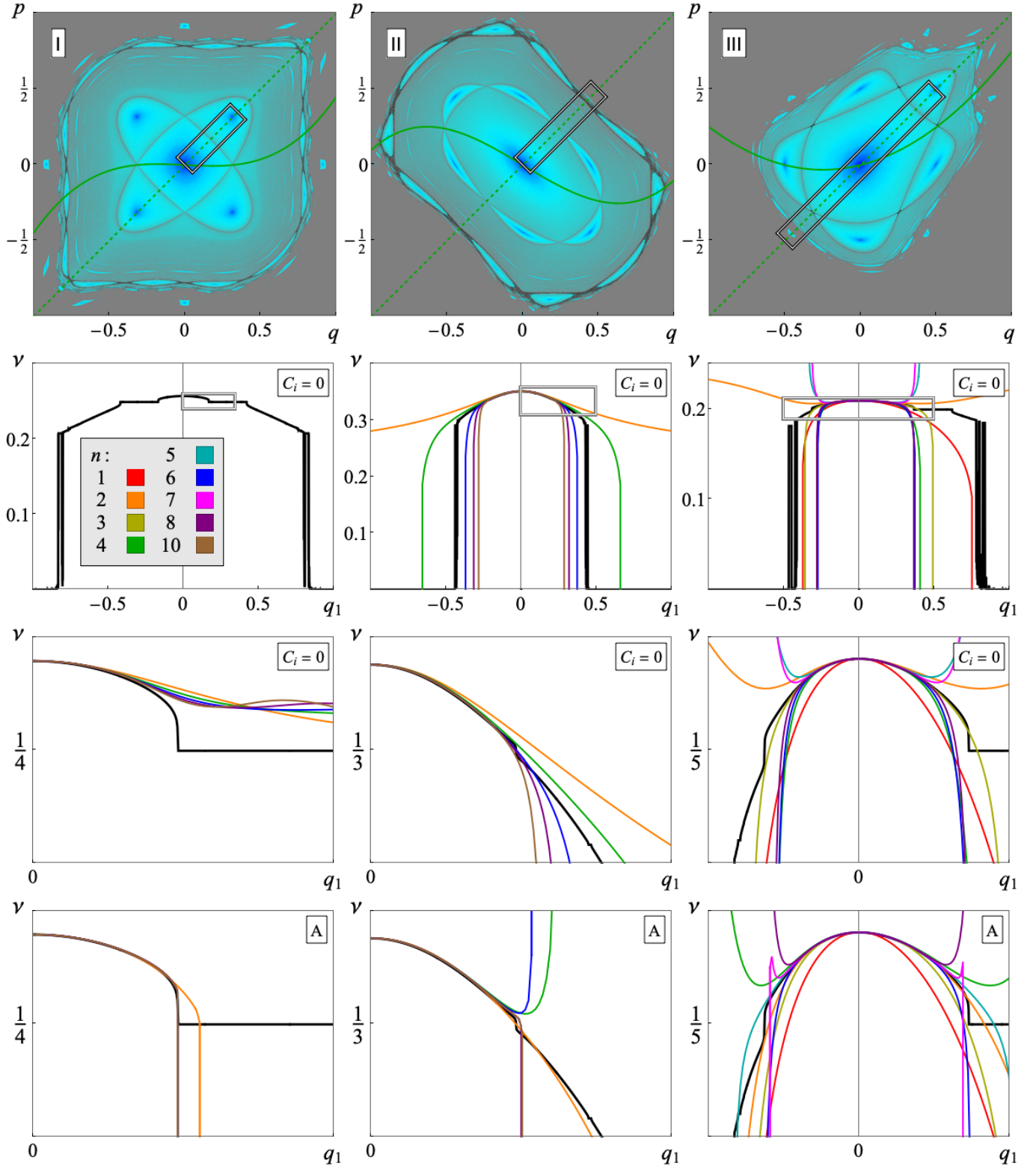


FIG. 3. Top row shows phase space portraits highlighted with the REM indicator for the Hénon cubic (I, II) and quadratic (III) mappings, corresponding to trace parameter values  $a = -1/10$ ,  $-6/5$ , and  $1/2$ , respectively. Dashed and solid green curves indicate the first and second symmetry lines. Second row presents rotation number  $\nu(q_1)$  as a function of the initial coordinate along the first symmetry line,  $\zeta_0 = (q_1, q_1)$ , obtained from numerical orbit tracking (black thick curves) and from non-averaged approximate invariants with  $C_i = 0$  (colored curves, labeled in the legend). Both rows include a white rectangle marking the region selected for magnification. Two bottom two rows contains close-up views of the selected region, showing the rotation number curves extracted from non-averaged invariants (third row) and after applying the averaging procedure (A) (fourth row).

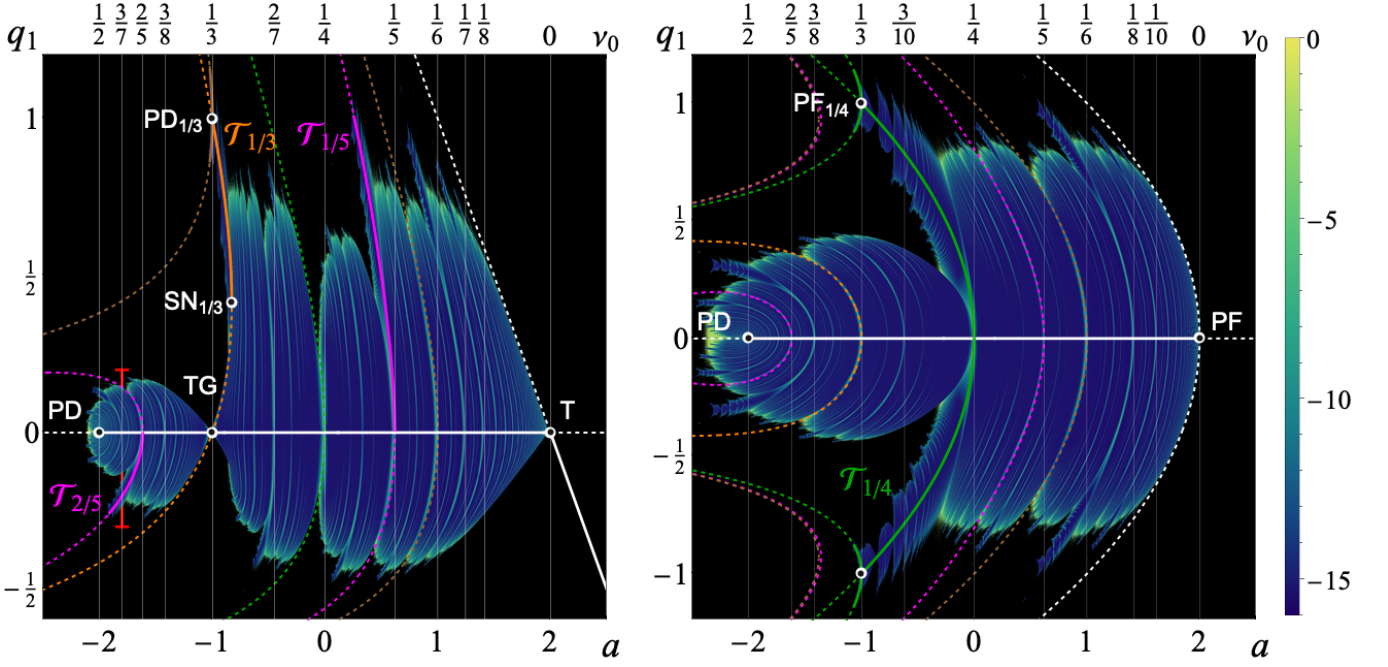


FIG. 4. Isochronous diagrams for the Hénon quadratic  $f(p) = ap + p^2$  (left) and cubic  $f(p) = ap + p^3$  (right) mappings. Each diagram displays the FMA index for stable initial conditions at different values of the trace parameter  $a$  across the coordinate  $q_1$ , measured along the first symmetry line  $l_1$ . The top axis provides corresponding values of the bare rotation number  $\nu_0$  for select low-order resonances. Additional curves indicate the locations of isolated fixed points (white) and periodic  $n$ -cycles ( $n \leq 6$ ), with solid for stable and dashed for unstable. Specifically, orange represents 3-cycles, green denotes 4-cycles, magenta corresponds to 5-cycles, and brown marks 6-cycles. Key bifurcations associated with these points are labeled with Latin letters: transcritical (T), pitchfork (PF), period doubling (PD), saddle-node (SN), and touch-and-go (TG). Arnold tongues, associated with some  $k$ -island chain bifurcations, are marked as  $\mathcal{T}_{\nu_0}$ . The red line segment at  $\nu_0 = 3/7$  (quadratic map) serves as a reference for Fig. 5.

### B. Simply connected region and chains of islands

One challenge in analyzing phase space plots lies in the choice of parameters. A “carefully” selected case study can create the illusion that a perturbation method is remarkably effective, while, conversely, cases where convergence can not be achieved (or has not yet been approached) may give the false impression that the method is unreliable. To mitigate this issue, we extend our study of Hénon mappings beyond individual phase space plots, shifting our focus to a mixed space representation that combines coordinates along a symmetry line with variations in the mapping parameter  $a$ . This broader perspective helps reveal underlying structures that may not be apparent in isolated phase space views. We refer to these diagrams as *isochronous* (along  $l_1$ ) and *period-doubling* (along  $l_2$ ), as they cut through all fixed points and 2-cycles, respectively. A dedicated manuscript [19] explores this topic in greater detail. Fig. 4 presents isochronous diagrams for the Hénon quadratic and cubic mappings, while Fig. 5 provides a corresponding phase space diagram, with the red line segment serving as a visual cue for comparison. The color scale represents the natural logarithm of the FMA index, capturing numerical diffusion in the rotation number:  $\log_{10}(10^{-16} + |\nu_I - \nu_{II}|)$  where  $\nu_{I,II}$  are the rotation numbers computed over the first and second halves of the iteration window.

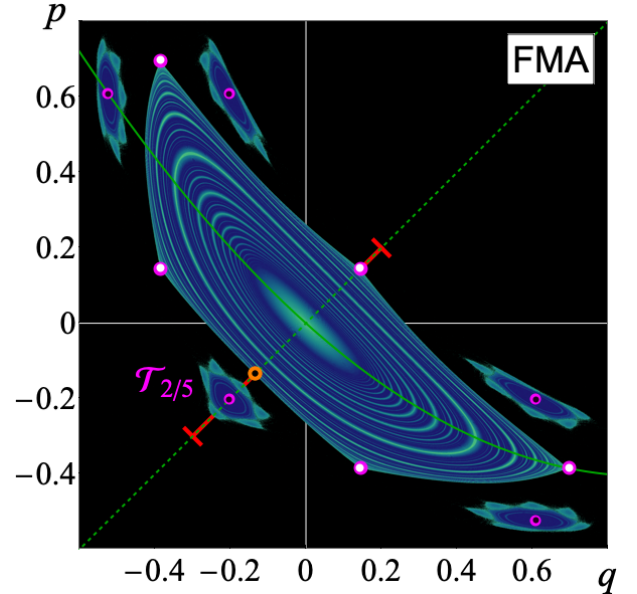


FIG. 5. Phase space diagram for the Hénon quadratic map at  $\nu_0 = 3/7$ . Magenta points indicate 5-cycles, with black-dot markers representing stable centers associated with a 5-island chain ( $\mathcal{T}_{2/5}$ ) and hollow markers indicating unstable solutions. Green curves represent the first (dashed) and second (solid) symmetry lines. The red line segment corresponds to Fig. 4.

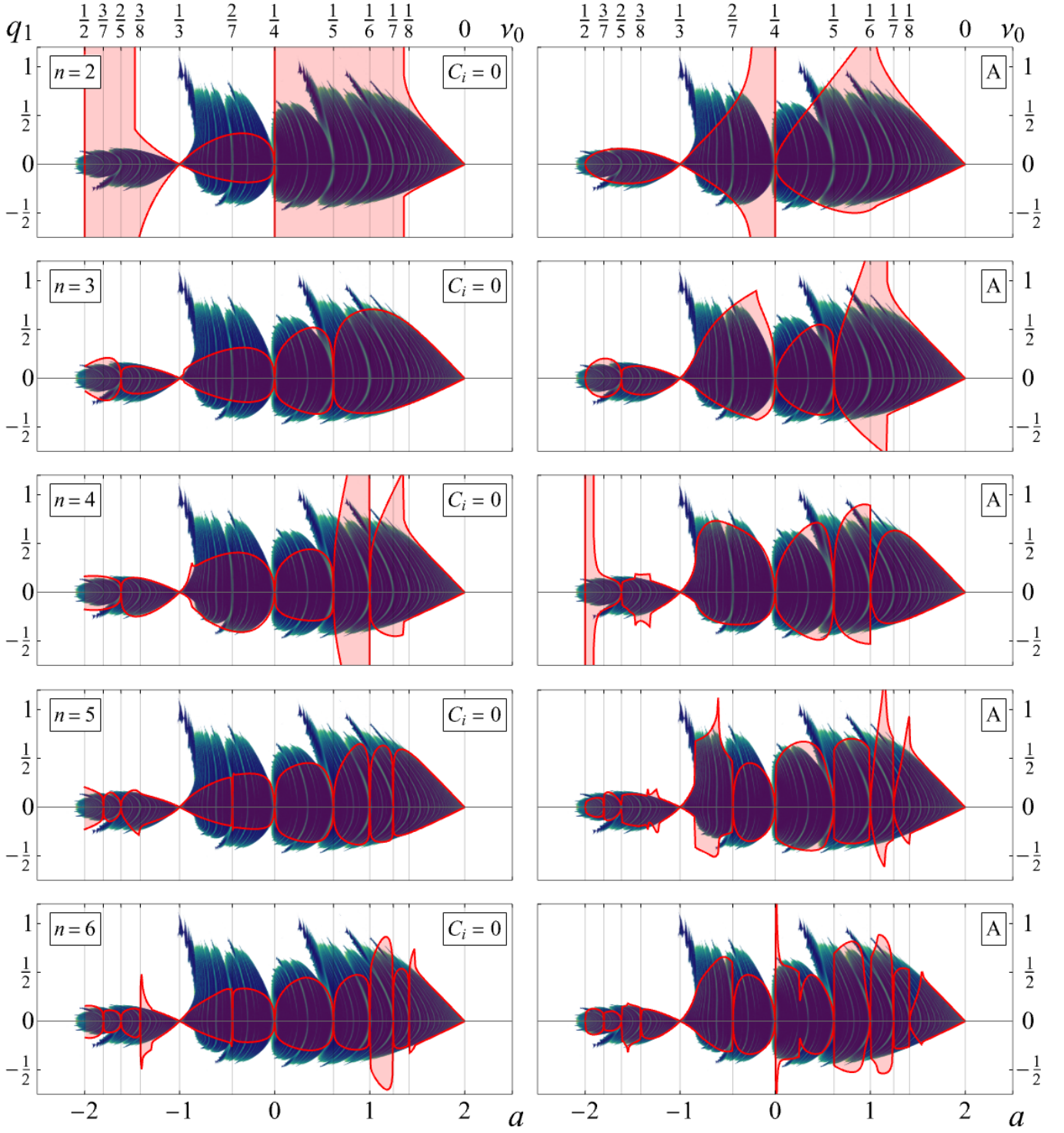


FIG. 6. Simply connected region (red) along the first symmetry line, extracted from non-averaged approximate invariants with  $C_i = 0$  and averaged invariants  $\langle \mathcal{K}^{(n)} \rangle$  (A), overlaid on the isochronous diagram for the Hénon quadratic map,  $f(p) = ap + p^2$ .

In this subsection, we explore the potential use of our approximate invariants to identify the locations of island chains. This question is particularly relevant in accelerator physics, where a detailed understanding of phase space is essential for improving the dynamic aperture — the region of stable trajectories around the origin or ref-

erence orbit. A larger dynamic aperture enables better particle capture and reduced beam losses, ultimately enhancing machine performance. Moreover, this knowledge aids in optimizing lattice designs for resonant extraction [15].

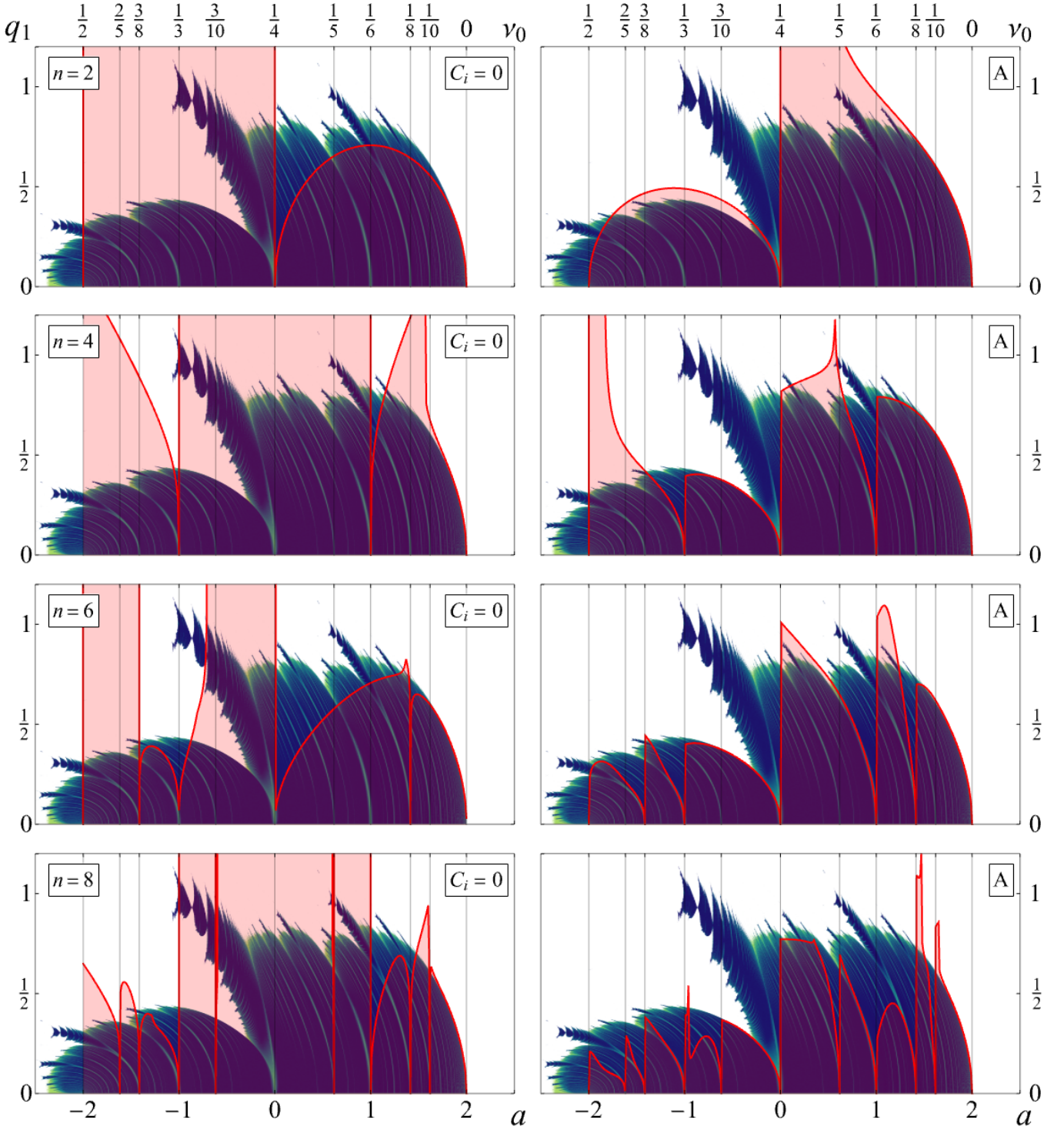


FIG. 7. Same as Fig. 6, but for the Hénon cubic map,  $f(p) = ap + p^3$ .

To investigate this, we analyze both the averaged approximate invariant  $\langle \mathcal{K}^{(n)} \rangle[p, q]$  and the non-averaged version  $\mathcal{K}^{(n)}[p, q]$ , where we once again set all  $C_i$  to zero to maintain consistency with prior calculations. From each, we extract the size of the simply connected region around the origin along the first symmetry line,  $l_1$ . This region is bounded by a *separatrix* — an invariant level set passing through a critical point, corresponding to an unstable fixed point (cycle) with associated invariant man-

ifolds. Depending on the geometry, the separatrix may intersect a symmetry line either directly or through a saddle point (see [19] for details). To visualize some of these concepts, we refer to Fig. 5. In this phase space plot, the dynamic aperture is roughly delineated by the unstable 5-cycle. The associated separatrix is pierced by the symmetry line  $l_1$  (green dashed): on the right through one of the cycle points, and on the left directly through the unstable manifolds (marked by the orange point).

Within this region, the dynamics appear quasi-integrable in the sense that no prominent island chains or large chaotic zones are visible at the given scale. However, unlike the previously discussed REM-highlighted phase space in Fig. 3, this quasi-integrable region exhibits numerous bands of lighter color. While these may not resemble island chains at first glance, they are indeed associated with orbits of rational rotation numbers, and the corresponding mode-locked regions (Arnold tongues) become visible upon closer magnification. While REM (along with SALI/GALI or Lyapunov exponent-based methods) is better suited for detecting chaos and other phase space features such as twistless orbits [19], the FMA indicator is more sensitive to resonant structures such as hyperbolic points, which justifies its use in this analysis.

In chaotic systems, a truly simply connected region does not exist, since island chains emerge at every scale. However, its boundary is well-defined within our approximate invariants. Figs. 6 and 7 provide the extracted boundary (shown as a red envelope curve) superimposed onto the isochronous diagrams from Fig. 4. If the fixed point at the origin is the only critical point of the invariant, no bounding separatrix exists and the dynamic aperture is effectively infinite; in such cases, no red curve is shown, and stability is indicated by the semi-transparent fill extending vertically.

Comparing the left-hand plots (non-averaged invariants with  $C_i = 0$ ) to the right-hand plots (averaged invariants), we observe an increasing number of “pinchings” in the red envelope as  $n$  increases. These collapses of the simply connected region correspond to resonances that appear in the expected orders. For general maps, including the quadratic Hénon map, the set of resonance values  $\{\nu_r^{(n)}\}$  appearing at order  $n$  are given by the left half of the Farey sequence:

$$\{\nu_r^{(n)}\} = \left\{ \frac{l}{m} \in F_{n+2} \mid 0 \leq \frac{l}{m} \leq \frac{1}{2} \right\}.$$

In the case of odd mappings, such as Hénon cubic map, the even resonances  $r_{2k}$  first appear at their corresponding even orders  $n = 2k - 2$ , while odd resonances  $r_{2k+1}$  arise along with even resonances of doubled period  $r_{4k+2}$  at order  $n = 4k$ :

$n$	$f(p)$	$f_{\text{odd}}(p)$
0	$r_1, r_2$	$(r_2, r_1)$
1	$r_1, r_2, r_3$	
2	$r_1, r_2, r_3, r_4$	$(r_2, r_1), r_4$
3	$r_1, r_2, r_3, r_4, r_5$	
4	$r_1, r_2, r_3, r_4, r_5, r_6$	$(r_2, r_1), r_4, (r_6, r_3)$
5	$r_1, r_2, r_3, r_4, r_5, r_6, r_7$	
6	$r_1, r_2, r_3, r_4, r_5, r_6, r_7, r_8$	$(r_2, r_1), r_4, (r_6, r_3), r_8$

A more detailed comparison shows that, while both approaches (with and without averaging) correctly identify the resonance locations, averaging once again yields significantly more accurate results.

Each plot in Figs. 6 and 7 is rich in information, and we encourage the reader to explore them in detail. To observe convergence, one can select a low-order resonance (using the complimentary top axis for  $\nu_0$ ) and locate the corresponding structure in the diagram — e.g., cyan lines corresponding to direct crossing of the separatrix, or Arnold tongues indicating island chains. By following the red envelope across increasing orders  $n$ , in case of averaging procedure, one sees it more closely conform to the resonance structure until it eventually “switches” to a higher-order resonance. Through systematic examination of these features, the advantage of the averaging procedure becomes clear.

### C. Square Matrix method

In this closing subsection, we compare our perturbative technique with the Square Matrix (SM) method [REF?]. The SM approach begins by reducing the dimensionality of the coefficient matrix. Then, through a Jordan decomposition, it derives a new set of approximate action-angle variables and an associated invariant. The deviation of this approximate action from constancy serves as a measure of stability and frequency fluctuation — analogous to the approximate invariance in our method.

To structure the comparison, we revisit the criteria that guided the development of our perturbative approach. In the first part of this manuscript, we focused on local convergence near the fixed point. Two central requirements were: (i) the rotation number should agree with its Lie series expansion at  $J = 0$ , and (ii) the method must remain valid even when the rotation number is rational — that is, at resonances. As Lie algebra methods are known to match numerical results near the origin, any approach failing to satisfy condition (i) should be considered inadequate. Throughout this work, we have demonstrated that there are infinitely many ways to construct approximate invariants (for  $n \geq 2$ ) that fulfill this requirement to a given order. The SM method appears to meet this criterion, which makes it a natural and interesting candidate for comparison. However, when it comes to condition (ii), our understanding is that the SM method is not inherently resonant. We were unable to derive approximate invariants using SM that resemble the resonant constructions discussed in the first part (see Subsection II D and Appendix 4, which includes the resonant normal forms). This suggests that the SM method lacks built-in mechanisms for treating resonant dynamics analytically.

The second set of criteria, relevant to large-amplitude dynamics and explored in the present part, includes: (iii) the ability to recover the exact invariant for integrable systems, and (iv) the capacity to capture (or even surpass) the island chains characteristic of chaotic systems. Our attempt to analytically recover the invariant for the integrable McMillan map using the SM method failed in the same way our own approach fails when the averaging

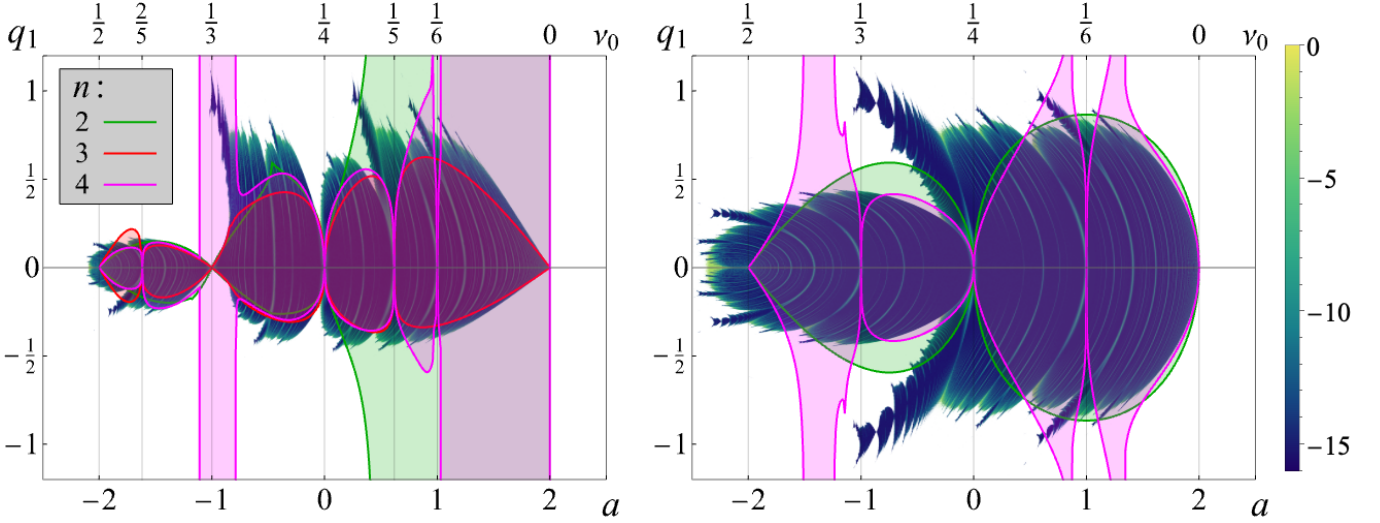


FIG. 8. Same as Figs. 6 (left plot) and 7 (right plot), but showing the boundaries of the simply connected region derived from the square matrix approximate invariants. Results from all available orders are displayed together, with each order indicated by a distinct color, as shown in the legend. Here,  $n$  denotes the perturbative order matching our PT method, while the matrix size is given by  $n + 2$ .

procedure is not applied: the invariant, instead of terminating properly at second order (as it should), grows with  $n$  and displays spurious resonant denominators. Nevertheless, we still proceed to apply the SM method to chaotic systems for comparison. Despite its limitations in the integrable regime, it remains worthwhile to assess how well SM captures features like island chains in more complex dynamical settings.

Fig. 8 revisits the isochronous diagrams for the quadratic and cubic Hénon maps, this time overlaying them with the simply connected regions extracted from the SM approximations. These are shown for orders corresponding to  $n = 2, 3, 4$  in our perturbative (PT) method. We omit the  $n = 1$  result to avoid redundancy, as it coincides exactly with the PT method without averaging and with vanishing  $C_1$  coefficient.

While our approximate invariants were obtained analytically for all orders, in the SM method we were only able to derive explicit analytical expressions for the lower orders shown. Attempts to extend the SM method numerically for this particular test were unfortunately unsuccessful. In our experience, as one approaches resonant values of the bare tune  $\nu_0$ , the numerical procedure becomes unstable, with resonant denominators diverging or “exploding,” leading to contamination of the plots with numerical artifacts. This limitation may reflect challenges in our implementation rather than the SM method itself. For this reason, we present only the most reliable results.

Overall, the qualitative behavior of the SM method closely parallels our PT results without averaging: as the order  $n$  increases, both methods consistently reveal resonances, following a Farey-like sequence. This is seen in the form of singularities or zero-crossings in the boundary of the simply connected region as  $\nu_0$  approaches rational

values. However, as the tune shifts away from resonance, the curves representing the SM-inferred regions increasingly deviate from the expected light-colored structures revealed by the FMA. Closer inspection of the diagrams confirms that PT with averaging consistently provides better global estimates of the boundary structure among the three methods. That said, even the averaged method is eventually limited by the persistent switching of dominant island chains, which ultimately reduces the size of the simply connected region.

Figs. 13 and 11 in Appendix B explore the SM method further by applying it to the specific case studies I – III introduced earlier in this section; in these examples, we were able to obtain numerically stable results up to  $n = 10$ . In case I, the SM method reveals the inner portion of the separatrix associated with the 4-island chain. Beginning at  $n = 6$ , the approximation becomes highly accurate — comparable to the PT result at  $n = 4$  with averaging, which already fully captures all four islands. For case II, the SM method again starts to approximate the inner part of the island chain from  $n = 6$  onward. However, even at  $n = 10$ , the method still noticeably deviates from the true locations of the unstable 3-cycles. In contrast, PT method with averaging reveals all six islands by  $n = 6$ , and at  $n \geq 14$  the approximation becomes nearly indistinguishable from the exact structure. In the more challenging case III, the pattern is similar: from  $n \geq 3$  the SM method begins to capture the inner region of the 5-island chain, gradually converging toward the correct geometry. Yet here too, the PT method with averaging appears to reach the true locations of the chain nodes more rapidly and with greater consistency; however, it is important to note that even our method encounters difficulties when it comes to consistently resolving fine island structures.

In all three cases, as  $n$  increases, the SM method seems to approach the dynamics of an integrable twist map inside the separatrix — but struggles to go beyond it and resolve structures outside that region. While a comprehensive study of the convergence properties of each method is beyond the scope of this work, our current observations suggest that PT with averaging tends to deliver more accurate predictions.

## V. CONCLUSIONS AND POSSIBLE GENERALIZATIONS

In this second part of the manuscript, we expanded our perturbative framework beyond the local dynamics near the fixed point to evaluate its performance across a broad range of nonlinear systems, including chaotic maps. Our primary focus was on the global structure of phase space and the ability of the method to describe key features such as rotation number, island chains, and approximate invariants with high fidelity.

The analysis was guided by two additional criteria, building upon the foundational requirements established in the first part. Specifically, we evaluated: (iii) whether the method can recover exact invariants in integrable systems, and (iv) whether it can accurately capture — and in some cases surpass — the island chains that dominate the phase space of chaotic systems.

Both objectives were met. For integrable systems, we demonstrated that the perturbative expansion, when properly averaged, (almost everywhere) converges to the exact invariants. In the non-integrable regime, we showed that the method successfully resolves nonlinear resonance structures, including island chains, and tracks their evolution across parameter space. The technique consistently produced reliable boundaries of the simply connected stable region. Notably, the rotation number — computed from the approximate invariant via Danilov’s theorem — closely follows the numerical tune extracted from orbit tracking across a wide range of initial conditions.

To place our method in context, we also compared it to the Square Matrix (SM) approach. While SM shares some formal similarities — particularly at low order — and seems to satisfy the essential requirement of local convergence near the fixed point, we found that it lacks a built-in mechanism for resonant expansions and struggles to recover the correct invariant in integrable systems without divergence. In chaotic systems, SM does resolve inner parts of island chains with increasing order, but it tends to underestimate their extent and fails to surpass separatrices. In contrast, our perturbative method with averaging consistently provided sharper boundaries and better alignment with true dynamical structures, especially near resonances.

The efficiency and generality of the method are further underscored by its application to several realistic

accelerator lattices in the final part of this series. All accelerator-related plots in this work were derived from a single unified object — the approximate invariant — which depends parametrically on the map coefficients. This demonstrates the method’s versatility and practicality as a diagnostic and design tool in beam dynamics. Despite the complexity of the underlying maps, the analytic construction of the invariant required only a modest number of perturbative terms, while averaging systematically improved both accuracy and convergence.

In summary, we have developed a perturbative technique that not only satisfies key theoretical benchmarks, but also performs remarkably well across integrable and chaotic regimes. It offers a transparent, analytic, and efficient framework for exploring nonlinear dynamics in symplectic maps, and provides a valuable complement to existing methods in accelerator physics and beyond.

## VI. ACKNOWLEDGMENTS

The authors would like to thank Taylor Nchako (Northwestern University) for carefully reading this manuscript and for her helpful comments. S.N. work is supported by the U.S. Department of Energy, Office of Science, Office of Nuclear Physics under contract DE-AC05-06OR23177. I.M. acknowledges that his work was partially supported by the Ministry of Science and Higher Education of the Russian Federation (project FWUR-2025-0004). S.K. is grateful to his supervisor, Prof. Young-Kee Kim (University of Chicago), for her valuable mentorship and continuous support.

Appendix A: Averaged approximate invariants for case studies I – III

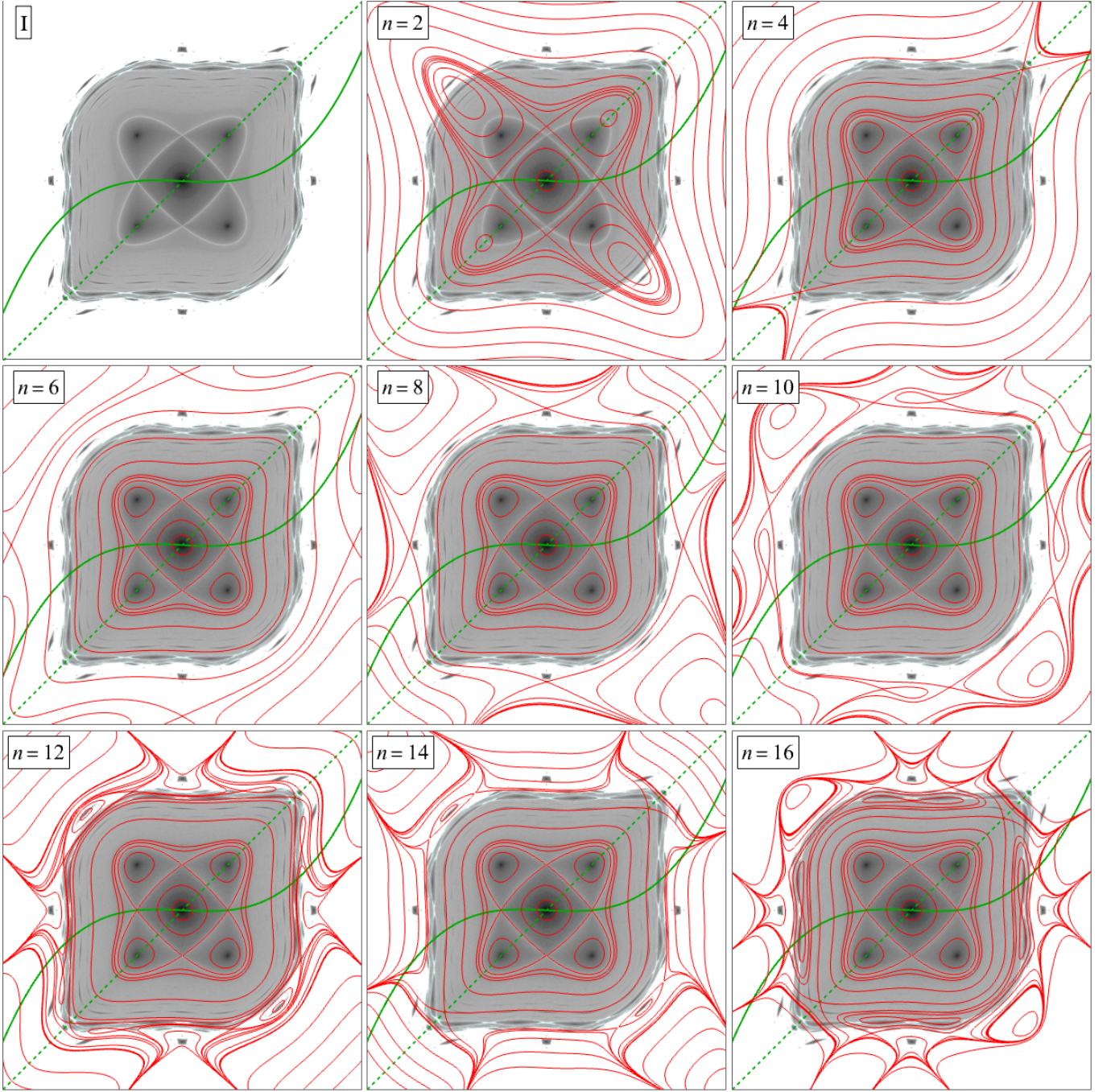


FIG. 9. Constant level sets of the averaged approximate invariant  $\langle \mathcal{K}^{(n)} \rangle[p, q]$  (red), superimposed on the phase-space portrait from Fig. 3. Shown for Case I: the cubic Hénon map with  $a = -1/10$ .

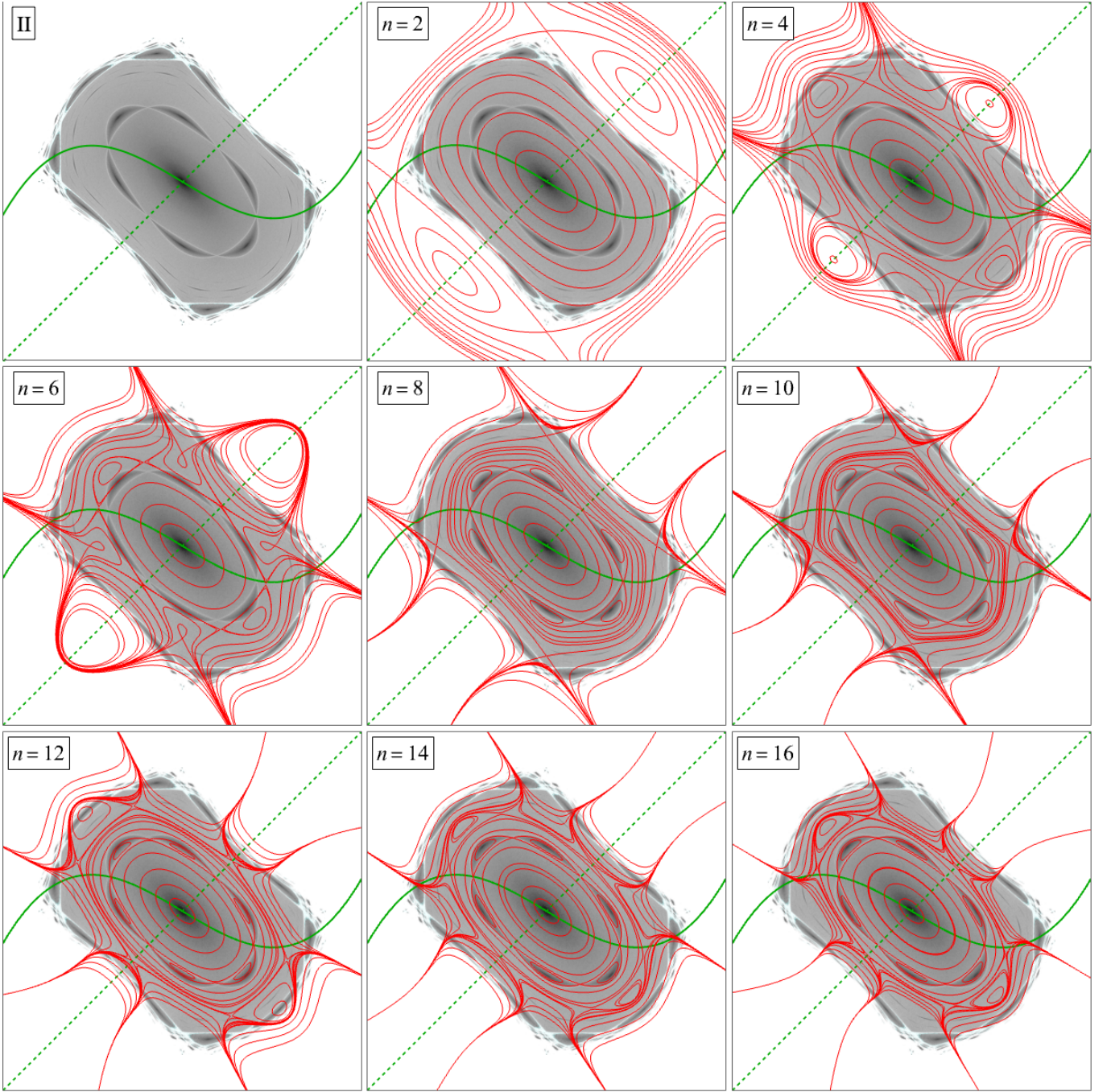


FIG. 10. Same as Fig. 9, but for Case II: the cubic Hénon map with  $a = -6/5$ .

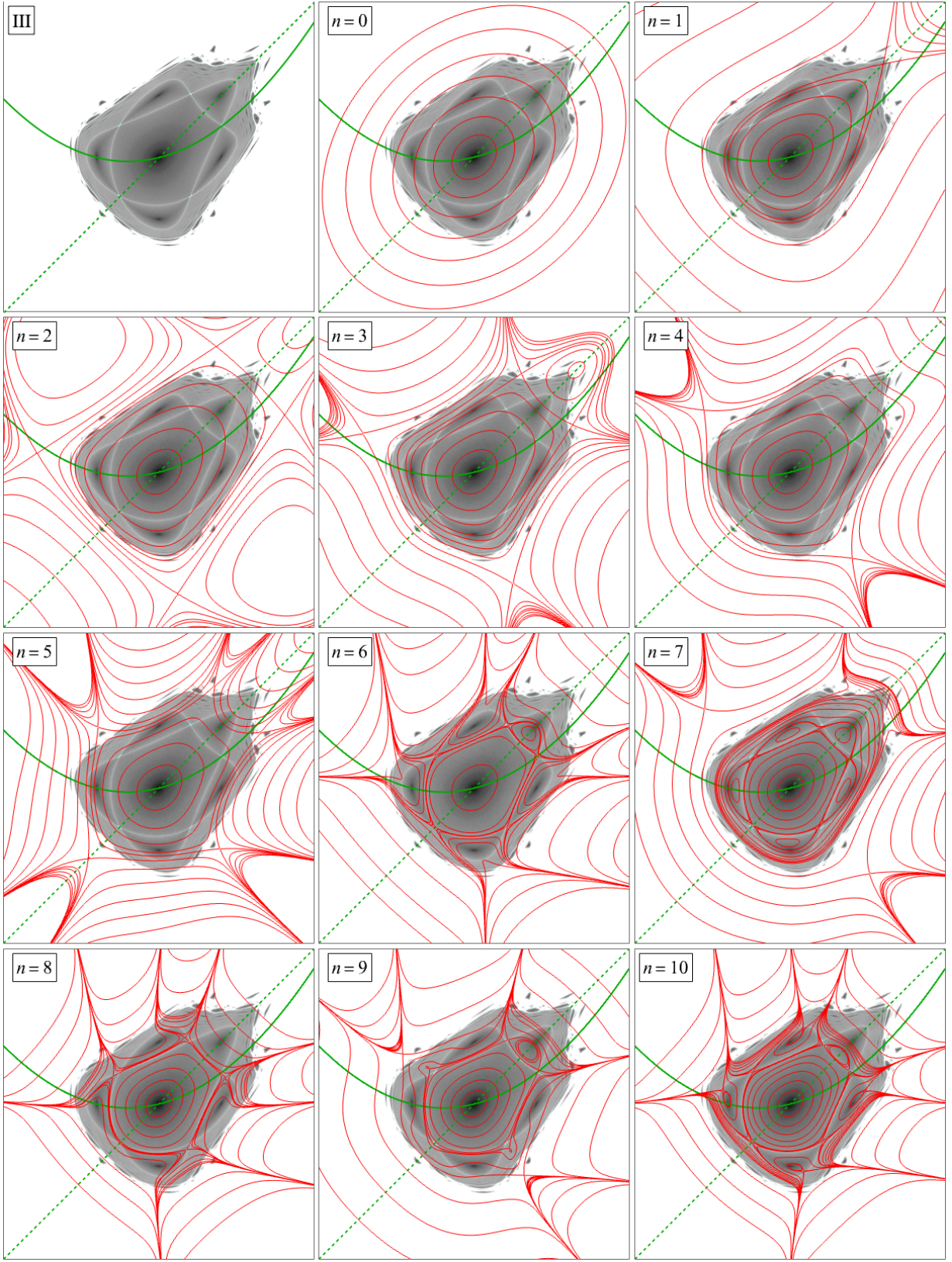


FIG. 11. Same as Fig. 9, but for Case III: the quadratic Hénon map with  $a = 1/2$ .

# Appendix B: Approximate Invariants via the Square Matrix Method

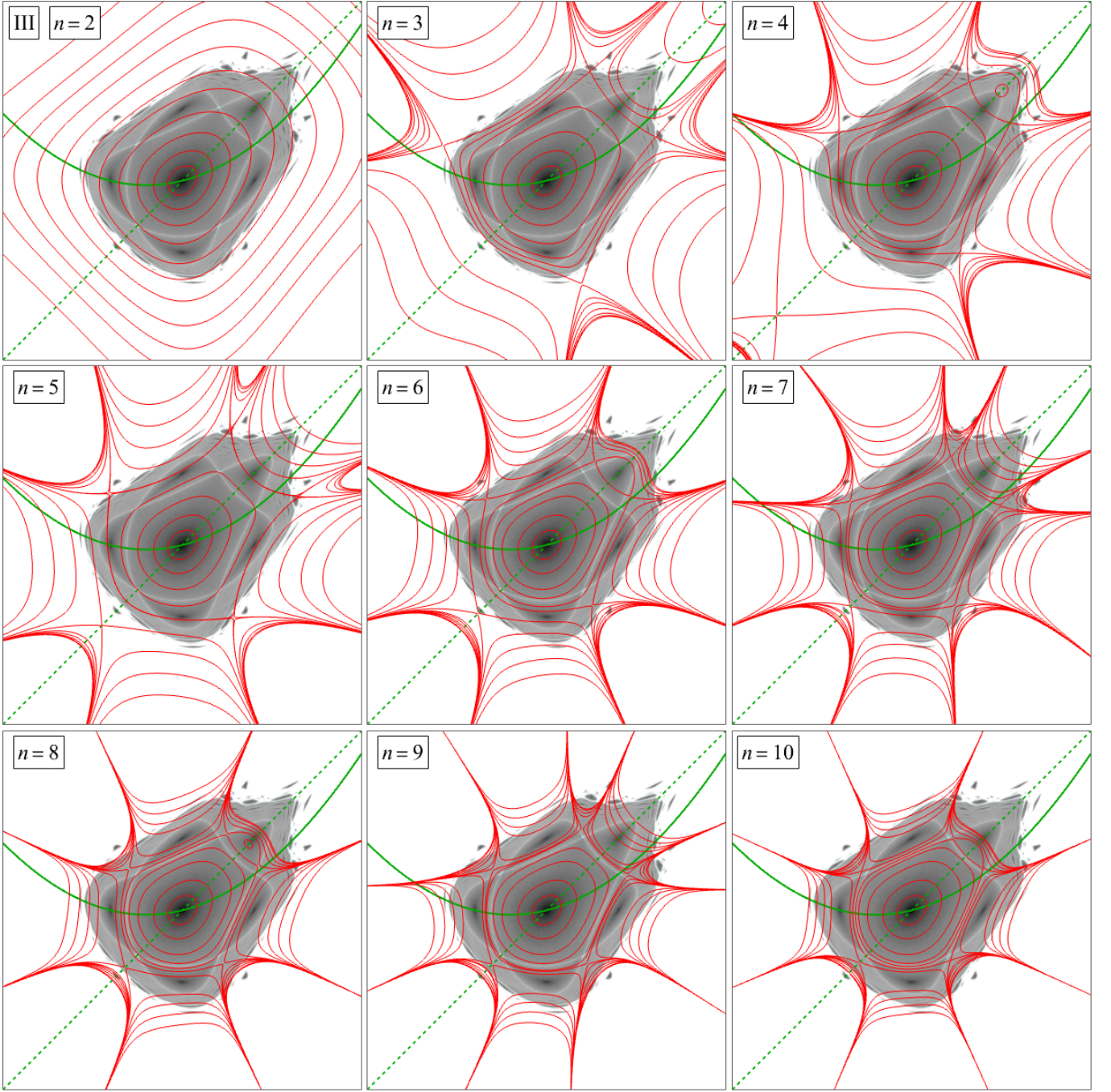


FIG. 12. Same as Fig. 11, but for the approximate invariants obtained via the square matrix method.

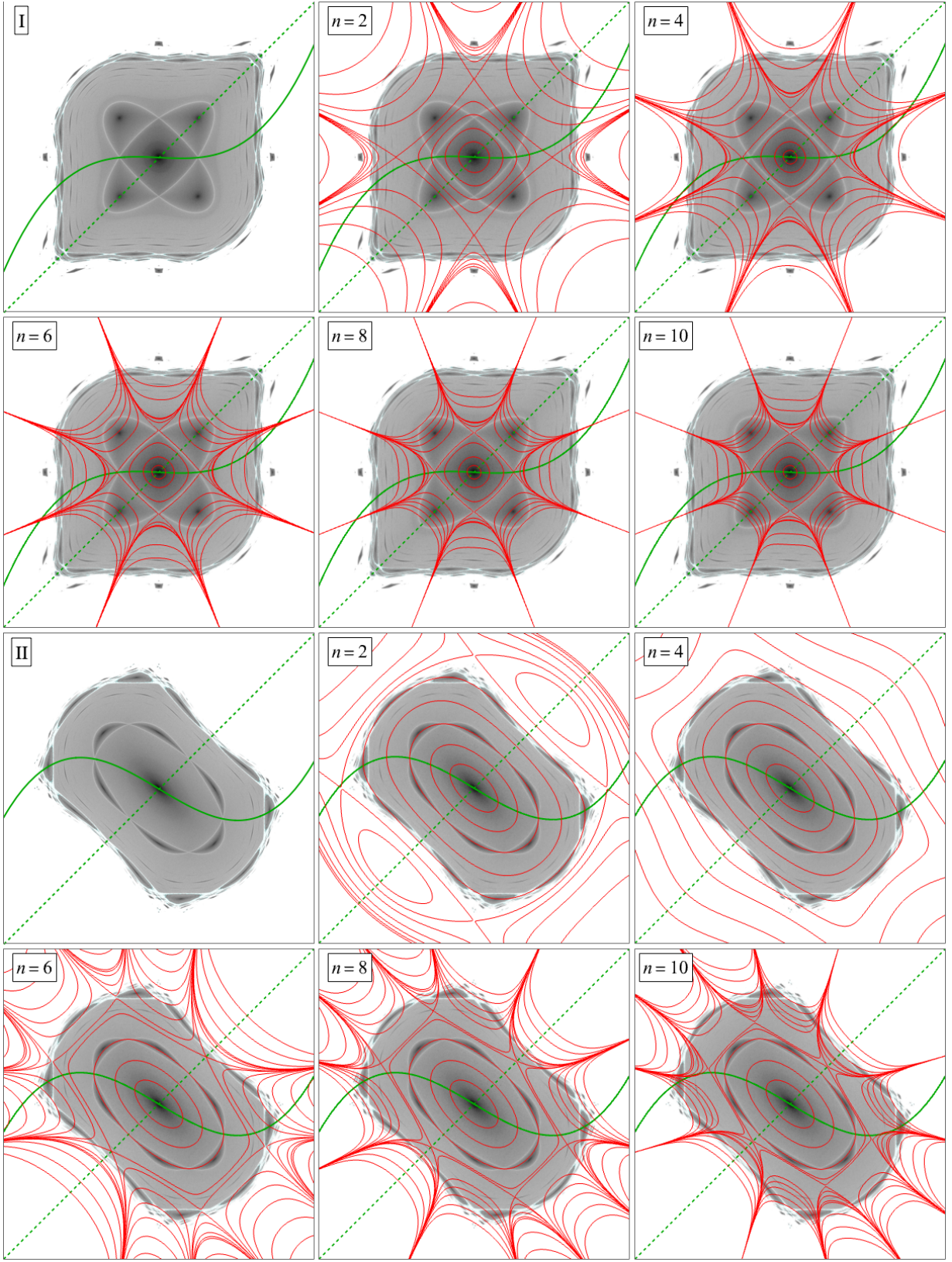


FIG. 13. Same as Figs. 9 and 10, but for the approximate invariants obtained via the square matrix method.

- 
- [1] V.I. Arnold and A. Avez, *Ergodic Problems of Classical Mechanics*, Advanced book classics (Addison-Wesley, 1989).
  - [2] A. I. Neishtadt V. I. Arnold, V. V. Kozlov, *Mathematical Aspects of Classical and Celestial Mechanics*, 2nd ed. (Springer Berlin, Heidelberg, 1997).
  - [3] Vladimir I. Arnold, *Dynamical Systems III*, 1st ed., Encyclopaedia of Mathematical Sciences (Springer Berlin, Heidelberg, 1988).
  - [4] J.A.G. Roberts and G.R.W. Quispel, “Chaos and time-reversal symmetry. order and chaos in reversible dynamical systems,” *Physics Reports* **216**, 63–177 (1992).
  - [5] E. Noether, “Invariante Variationsprobleme,” *Nachrichten von der Gesellschaft der Wissenschaften zu Göttingen, Mathematisch-Physikalische Klasse* **1918**, 235–257 (1918).
  - [6] Andrey Nikolaevich Kolmogorov, “On conservation of conditionally periodic motions for a small change in Hamilton’s function,” (1954) pp. 527–530.
  - [7] Vladimir I. Arnold, “Proof of a theorem of A. N. Kolmogorov on the preservation of conditionally periodic motions under a small perturbation of the Hamiltonian,” *Russian Mathematical Surveys* **18**, 9–36 (1963).
  - [8] Jürgen Moser, “On invariant curves of area-preserving mapping of an annulus,” *Matematika* **6**, 51–68 (1962).
  - [9] Edwin M. McMillan, “A problem in the stability of periodic systems,” in *Topics in modern physics. A Tribute to Edward U. Condon*, edited by W. E. Brittin and H. Odabasi (Colorado Associated University Press, Boulder, CO, 1971) pp. 219–244.
  - [10] Yuri B. Suris, “Integrable mappings of the standard type,” *Functional Analysis and Its Applications* **23**, 74–76 (1989).
  - [11] Michel Hénon, “Numerical study of quadratic area-preserving mappings,” *Quarterly of Applied Mathematics* **27**, 291–312 (1969).
  - [12] D. Sterling, H.R. Dullin, and J.D. Meiss, “Homoclinic bifurcations for the Hénon map,” *Physica D: Nonlinear Phenomena* **134**, 153–184 (1999).
  - [13] H.R. Dullin, J.D. Meiss, and D. Sterling, “Generic twistless bifurcations,” *Nonlinearity* **13**, 203 (2000).
  - [14] H.R. Dullin and J.D. Meiss, “Generalized Hénon maps: the cubic diffeomorphisms of the plane,” *Physica D: Nonlinear Phenomena* **143**, 262–289 (2000).
  - [15] Tim Zolkin, Sergei Nagaitsev, and Ivan Morozov, “Dynamics of McMillan mappings I. McMillan multipoles,” (2024), arXiv:2405.05652 [nlin.SI].
  - [16] Tim Zolkin, Sergei Nagaitsev, Ivan Morozov, Sergei Kladov, and Young-Kee Kim, “Dynamics of McMillan mappings III. Symmetric map with mixed nonlinearity,” (2024), arXiv:2410.10380 [nlin.SI].
  - [17] Ernest D. Courant and Hartland S. Snyder, “Theory of the alternating-gradient synchrotron,” *Annals of Physics* **3**, 1–48 (1958).
  - [18] Apostolos Iatrou and John A. G. Roberts, “Integrable mappings of the plane preserving biquadratic invariant curves II,” *Nonlinearity* **15**, 459–489 (2002).
  - [19] Tim Zolkin, Sergei Nagaitsev, Ivan Morozov, Sergei Kladov, and Young-Kee Kim, “Isochronous and period-doubling diagrams for symplectic maps of the plane,” (2024), arXiv:2412.05541 [nlin.CD].